FOUNDATIONS
ADVANCES

ISSN: 2053-2733
journals.iucr.org/a

# Introduction of a weighting scheme for the X-ray restrained wavefunction approach: advantages and drawbacks

**Giovanni Macetti and Alessandro Genoni**

*Acta Cryst.* (2023). A**79**, 25–40

Acta Cryst A FOUNDATIONS ADVANCES
ISSN 2053-2733

# Introduction of a weighting scheme for the X-ray restrained wavefunction approach: advantages and drawbacks

Giovanni Macetti and Alessandro Genoni*

Université de Lorraine and CNRS, Laboratoire de Physique et Chimie Théoriques, 1 Boulevard Arago, Metz, F-57078, France. *Correspondence e-mail: alessandro.genoni@univ-lorraine.fr

Received 4 July 2022
Accepted 23 October 2022

Edited by A. Altomare, Institute of Crystallography - CNR, Bari, Italy

**Keywords:** X-ray restrained/constrained wavefunction; weighting scheme; reflection distribution; quantum crystallography.

**Supporting information**: this article has supporting information at journals.iucr.org/a

In a quite recent study [Genoni *et al.* (2017). *IUCrJ*, **4**, 136–146], it was observed that the X-ray restrained wavefunction (XRW) approach allows a more efficient and larger capture of electron correlation effects on the electron density if high-angle reflections are not considered in the calculations. This is due to the occurrence of two concomitant effects when one uses theoretical X-ray diffraction data corresponding to a single-molecule electron density in a large unit cell: (i) the high-angle reflections are generally much more numerous than the low- and medium-angle ones, and (ii) they are already very well described at unrestrained level. Nevertheless, since high-angle data also contain important information that should not be disregarded, it is not advisable to neglect them completely. For this reason, based on the results of the previous investigation, this work introduces a weighting scheme for XRW calculations to up-weight the contribution of low- and medium-angle reflections, and, at the same time, to reasonably down-weight the importance of the high-angle data. The proposed strategy was tested through XRW computations with both theoretical and experimental structure-factor amplitudes. The tests have shown that the new weighting scheme works optimally if it is applied with theoretically generated X-ray diffraction data, while it is not advantageous when traditional experimental X-ray diffraction data (even of very high resolution) are employed. This also led to the conclusion that the use of a specific external parameter $\lambda_J$ for each resolution range might not be a suitable strategy to adopt in XRW calculations exploiting experimental X-ray data as restraints.

## 1. Introduction

Quantum crystallography is an emerging field of science having the goal of investigating properties and phenomena that are crucial for or occur in the crystalline state and that can be explained only through the laws of quantum mechanics (Genoni, Bučinský *et al.*, 2018; Grabowsky *et al.*, 2017, 2020; Massa & Matta, 2018; Genoni & Macchi, 2020; Macchi, 2020, 2022). There are different ways to achieve this objective. For example, we mention the application of multipole model techniques (Stewart, 1976; Hansen & Coppens, 1978) or maximum entropy methods (Sakata & Sato, 1990; Roversi *et al.*, 1998; van Smaalen & Netzel, 2009) for the determination of experimental charge densities, the exploitation of computational chemistry/physics software [such as *CRYSTAL* (Dovesi, Orlando *et al.*, 2014; Dovesi, Erba *et al.*, 2018) or *Quantum Espresso* (Giannozzi *et al.*, 2017)] to perform periodic *ab initio* computations, or the use of quantum chemical topology techniques (Bader, 1990; Bader & Gatti, 1998; Becke & Edgecombe, 1990; Silvi & Savin, 1994; Kohout, 2004; Blanco *et al.*, 2005; Johnson *et al.*, 2010) to analyse the obtained experimental or theoretical electron-density distributions.

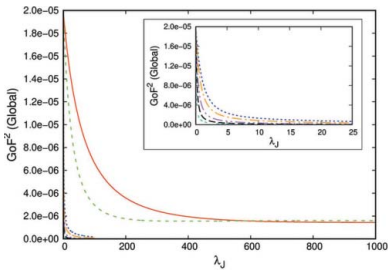

In addition to the above-mentioned strategies, there are other emerging quantum crystallographic methods characterized by a simultaneous and strict interplay between the results of quantum chemistry calculations and crystallographic experiments. This is generally accomplished in two ways. On the one hand, the quantum mechanical calculations are directly exploited in the determination of crystal structures to get better structural models compared with those resulting from traditional refinement approaches; this is what is done in the well known Hirshfeld atom refinement (HAR) technique (Jayatilaka & Dittrich, 2008; Capelli *et al.*, 2014; Kleemiss *et al.*, 2021). On the other hand, there are also methods in which the results of crystallographic experiments are directly used in quantum mechanical calculations to try to enrich the information content of the wavefunction; this is the case of the X-ray restrained/constrained wavefunction strategy[1] (Jayatilaka, 1998; Jayatilaka & Grimwood, 2001), which is the main topic of this work.

The X-ray restrained wavefunction (XRW) method is a technique originally introduced by Jayatilaka (1998), Jayatilaka & Grimwood (2001) to determine wavefunctions compatible with sets of experimentally collected X-ray structure-factor amplitudes. As will be discussed in more detail in Section 2 of this paper, the approach searches for wavefunctions that minimize the energy of the system under examination and that simultaneously maximize the statistical agreement between computed and experimental/reference X-ray diffraction data.

Initially developed in the framework of the restricted Hartree–Fock (HF) formalism (Jayatilaka, 1998; Jayatilaka & Grimwood, 2001; Grimwood & Jayatilaka, 2001; Bytheway, Grimwood & Jayatilaka, 2002; Bytheway, Grimwood, Figgis *et al.*, 2002; Grimwood *et al.*, 2003), the Jayatilaka technique has known a quite diversified methodological development over the years. At first, the strategy was extended to the unrestricted HF case (Hudák *et al.*, 2010) and to density functional theory (DFT) (Jayatilaka, 2012). At a later stage, it was combined with relativistic approaches, such as the Douglas–Kroll–Hess and infinite-order two-component relativistic techniques (Hudák *et al.*, 2010; Bučinský *et al.*, 2016). Moreover, it was coupled with the Stoll method (Stoll *et al.*, 1980) for the determination of extremely localized molecular orbitals (ELMOs) (Genoni, 2013*a*,*b*; Dos Santos *et al.*, 2014; Genoni & Meyer, 2016) and, more recently, also with multi-determinant wavefunction techniques of valence-bond type (Genoni, 2017; Casati *et al.*, 2017; Genoni, Franchini *et al.*, 2018; Genoni *et al.*, 2019). Electron densities and molecular orbitals resulting from XRW calculations were also interestingly used to embed quantum mechanical calculations through multi-scale fully quantum mechanical embedding methods (Ricardi *et al.*, 2020; Macetti, Macchi & Genoni, 2021) such as the frozen density embedding theory (FDET) (Wesolowski & Warshel, 1993; Wesołowski, 2008; Wesolowski *et al.*, 2015) and the quantum mechanics/extremely localized molecular orbital (QM/ELMO) approach (Macetti & Genoni, 2019; Macetti *et al.*, 2020; Macetti & Genoni, 2020; Wieduwilt *et al.*, 2021; Macetti, Wieduwilt *et al.*, 2021; Macetti & Genoni, 2021*a*,*b*,*c*). Finally, for the sake of completeness, it is worth mentioning that the XRW technique was also successfully coupled with HAR, giving rise to the so-called X-ray wavefunction refinement (XWR) technique, a strategy that allows the simultaneous refinement of molecular orbital coefficients and structural parameters (*i.e.* atomic positions and thermal parameters) using experimental X-ray diffraction data (Woińska *et al.*, 2017).

In parallel to the methodological development described in the previous paragraph, the Jayatilaka technique was also fruitfully exploited to investigate interesting chemical and physical problems. For instance, since the beginning it was exploited to extract additional information on chemical bonding from X-ray diffraction data. This was the case of the pioneering study carried out by Jayatilaka & Grimwood (2004), who computed electron localization functions (ELFs) resulting from XRW computations and compared them with corresponding ELFs obtained by means of gas-phase calculations to highlight crystal field effects. Similar studies were also those in which Grabowsky and coworkers determined localizability indicator domains associated with XRW wavefunctions to study the influence of the crystal environment on a series of epoxide derivatives (Grabowsky *et al.*, 2010) and to gain some insights into the reactivities of $\alpha$,$\beta$-unsaturated carbonyl and hydrazone compounds (Grabowsky *et al.*, 2011). Along the same line, the Grabowsky group also exploited the XRW approach together with different bonding descriptors to investigate specific chemical problems from different perspectives, for example to investigate hypervalency in sulfur dioxide and in phosphate, sulfate and perchlorate anions (Grabowsky *et al.*, 2012; Fugel *et al.*, 2019). Analogous efforts were made by Thomas and collaborators to study the properties of chalcogen bonds by performing chemical topology analyses on electron densities resulting from XRW computations (Thomas *et al.*, 2015; Grabowsky *et al.*, 2020). Moreover, the XRW approach was also used in solid-state and materials science studies. For instance, XRW computations were carried out to obtain (hyper)polarizabilities and refractive indices of molecular crystals from experimental X-ray diffraction data (Whitten *et al.*, 2006; Jayatilaka *et al.*, 2009). This was the first evidence that XRW wavefunctions can capture the effects of the crystal environment when experimental X-ray diffraction data are used as restraints, which was afterwards confirmed by Hickstein and collaborators in their studies on non-linear optical properties of molecular crystals (Hickstein *et al.*, 2013; Cole & Hickstein, 2013) and, above all, by a more recent investigation that exclusively aimed to fully explore this problem (Ernst *et al.*, 2020).

The above-mentioned work by Ernst and collaborators on the possibility of incorporating crystal field effects through XRW calculations can be considered as the follow-up of an

[1] The technique was originally known as the 'X-ray constrained wavefunction' approach. However, as already observed in the literature, in this technique the experimental data act as restraints in the crystallographic sense (Grabowsky *et al.*, 2017; Ernst *et al.*, 2020; Macetti, Macchi & Genoni, 2021; Genoni, 2022). Therefore, the method is better referred to as the 'X-ray restrained wavefunction' approach, and this is the term we use throughout the text.

earlier study on the capability of XRW wavefunctions to capture electron corelation effects on the electron density (Genoni *et al.*, 2017). In that investigation it was observed that correlation effects can be effectively incorporated by means of XRW computations, but this is generally clearer and more effective when only medium- and low-angle reflections are considered as restraints. This fact was rationalized by observing that, in the case of theoretically generated X-ray diffraction data corresponding to a single-molecule electron density in a large unit cell, the high-angle reflections are much more numerous than the other ones and already very well described at an unrestrained level. The consequence is that the significant electron correlation effects contained in the low- and medium-angle data cannot be fully captured if the high-angle structure-factor amplitudes are fully considered in the usual squared goodness-of-fit ($GoF^2$) which is used in the expression of the Jayatilaka functional to be minimized (see Section 2 for more details). Interestingly, recent works on HAR have also shown that low-angle reflections are more important and crucial for the description of relativistic effects (Pawlędzio *et al.*, 2022*a*,*b*).

Therefore, the previous result prompted us to propose a new and simple weighting scheme based on the uneven distribution of the X-ray data in the resolution shells. In principle, this would allow us to reasonably reduce the importance of the high-angle data while simultaneously increasing the weight of the low- and medium-angle reflections. A re-equilibration of the problem described in the previous paragraph is thus expected, at least in the case of theoretically generated X-ray structure-factor amplitudes. In this work, this new weighting scheme will be presented and then tested for XRW calculations performed with both theoretical and experimental X-ray diffraction data.

The paper is organized as follows. In the next section, after briefly reviewing the main aspects of the XRW approach, we will describe the proposed weighting scheme from the theoretical point of view. Afterwards, in Section 3, we will provide all the details of the performed computations, while in Section 4 we will present and discuss the obtained results. Finally, in the last part of the work, we will draw our conclusions, indicating when the use of the proposed weighting scheme could be advantageous to increase the performances of the XRW calculations and when, in contrast, it should not be applied.

## 2. Theory

### 2.1. XRW method

The XRW approach relies on three fundamental assumptions (Jayatilaka, 1998; Jayatilaka & Grimwood, 2001): (i) it formally works with a fictitious molecular crystal consisting of non-interacting units; (ii) the considered artificial non-interacting molecular crystal is characterized by an overall electron density that is equal to that of the corresponding real system made of interacting units (see below); (iii) all the crystal units are described by independent wavefunctions that are formally identical and related to each other through the crystal symmetry operations, which will hereafter be indicated by the roto-translations $\{\mathbf{Q}_k, \mathbf{q}_k\}_{k=1}^{N_m}$ (with $N_m$ the number of symmetry-equivalent positions in the crystal unit cell).

Based on the previous assumptions, the unit-cell electron density of the investigated system can be expressed only as a function of the electron-density distribution $\rho_0(\mathbf{r})$ of the reference crystal unit:

$$\rho_{\rm cell}(\mathbf{r}) = \sum_{k=1}^{N_m} \rho_k(\mathbf{r}) = \sum_{k=1}^{N_m} \rho_0\left[\mathbf{Q}_k^{-1}(\mathbf{r} - \mathbf{q}_k)\right]. \quad (1)$$

The electron density $\rho_0(\mathbf{r})$ clearly corresponds to the wavefunction $\Psi_0$ of the reference crystal unit, which, in the XRW calculations, is obtained by minimizing the following functional:

$$J[\Psi_0] = E[\Psi_0] + \lambda_J \, GoF^2[\Psi_0], \quad (2)$$

where $E[\Psi_0]$ is the gas-phase electronic energy of the molecular unit under examination (with $[\Psi_0]$ indicating the functional dependence on $\Psi_0$), and $GoF^2[\Psi_0]$ the statistical agreement between calculated and experimental/reference structure-factor amplitudes [note that here we decided to follow the terminology recently introduced by Davidson *et al.* (2022*a*,*b*), who correctly advised use of the term $GoF^2$ instead of $\chi^2$]:

$$GoF^2[\Psi_0] = \frac{1}{N_r - N_p} \sum_{\mathbf{h}} \frac{\left(\eta \, F_{\mathbf{h}}^{\rm calc}[\Psi_0] - F_{\mathbf{h}}^{\rm obs}\right)^2}{\sigma_{\mathbf{h}}^2}, \quad (3)$$

with $N_r$ as the number of structure-factor amplitudes, $N_p$ the number of adjustable parameters, $\mathbf{h} = (h, k, l)$ the triad of Miller indices associated with the reflection, $\eta$ the $\mathbf{h}$-independent scale factor that puts the calculated structure-factor amplitudes $\{F_{\mathbf{h}}^{\rm calc}\}$ on the same scale as the experimental/reference ones $\{F_{\mathbf{h}}^{\rm obs}\}$, and $\sigma_{\mathbf{h}}$ the experimental uncertainty associated with $F_{\mathbf{h}}^{\rm obs}$.

In equation (2), the second term on the right-hand side guarantees that the electron density of the assumed fictitious non-interacting molecular crystal eventually becomes identical to the global electron density of the corresponding interacting system, obviously within the limit of the uncertainties associated with the measurements when experimental X-ray diffraction data are used in the calculations. Finally, again in equation (2), it is worth pointing out that $\lambda_J$ is an external parameter that modulates the weight of the external restraints and that is gradually increased (*i.e.* not refined) during the XRW calculations [note that we decided to use the notation $\lambda_J$ to better distinguish the external parameter of the Jayatilaka approach from the wavelength of the radiation, which will be considered in other parts of the text, and which will be simply indicated with $\lambda$]. The problem of determining the correct value of $\lambda_J$ is still unsolved within the quantum crystallography community and particularly among the developers of the XRW approach. To this end, different criteria have been introduced and tested over the years (Davidson *et al.*, 2022*a*) and a reformulation of the Jayatilaka method has been recently proposed (Genoni, 2022). As will be indicated again in the section dedicated to the computational

details, in this work we chose to halt the XRW computations at the $\lambda_J$ values for which the SCF (self-consistent field) processes stopped converging.

So far, no indication has been given on the functional form that the reference crystal unit wavefunction $\Psi_0$ should have. This wavefunction *ansatz* is very important because it determines the type of XRW method. Since in this work we will exclusively work with the XRW technique in the framework of the HF formalism, here we assume that the reference crystal unit wavefunction has the form of a single Slater determinant. If we rely on this hypothesis and if we introduce the total scattering operator for a $2N$-electron system

$$\hat{\Im}_{\mathbf{h}} = \sum_{j=1}^{2N}\sum_{k=1}^{N_m} \exp\left[i2\pi(\mathbf{Q}_k\mathbf{r}_j + \mathbf{q}_k)\cdot(\mathbf{Gh})\right] = \sum_{j=1}^{2N}\hat{I}_{\mathbf{h}}(\mathbf{r}_j) = \sum_{j=1}^{2N}\hat{I}_{\mathbf{h},R}(\mathbf{r}_j) + i\,\hat{I}_{\mathbf{h},C}(\mathbf{r}_j), \quad (4)$$

with $\mathbf{G}$ as the reciprocal-lattice matrix, it is possible to show that looking for the wavefunction $\Psi_0$ that minimizes functional (2) is equivalent to solving the following modified HF equations:

$$\hat{F}_{\mathrm{XRW}}\phi_i(\mathbf{r}) = [\hat{F} + \lambda_J\hat{v}_{\mathrm{XRW}}]\phi_i(\mathbf{r}) = \epsilon_i\phi_i(\mathbf{r}), \quad (5)$$

where $\hat{F}$ is the usual Fock operator used in quantum chemistry calculations and $\hat{v}_{\mathrm{XRW}}$ is the additional operator that accounts for the influence of the restraints given by the experimental/reference data and that can be expressed as follows:

$$\hat{v}_{\mathrm{XRW}} = \sum_{\mathbf{h}} K_{\mathbf{h}}\left[\mathrm{Re}\{F_{\mathbf{h}}^{\mathrm{calc}}\}\,\hat{I}_{\mathbf{h},R} + \mathrm{Im}\{F_{\mathbf{h}}^{\mathrm{calc}}\}\,\hat{I}_{\mathbf{h},c}\right], \quad (6)$$

with the $\mathbf{h}$-dependent constant $K_{\mathbf{h}}$ given by

$$K_{\mathbf{h}} = \frac{2\eta}{N_r - N_p}\,\frac{\eta\,F_{\mathbf{h}}^{\mathrm{calc}} - F_{\mathbf{h}}^{\mathrm{obs}}}{\sigma_{\mathbf{h}}^2\,F_{\mathbf{h}}^{\mathrm{calc}}}. \quad (7)$$

The XRW strategy outlined above was implemented in an in-house-modified version of the *Gaussian09* quantum chemistry package (Frisch *et al.*, 2009).

### 2.2. Weighting scheme

As mentioned in Section 1, in a previous study it was observed that the XRW method allows the electron correlation effects on the electron density to be captured more efficiently and to a larger extent when only low- and medium-angle X-ray diffraction data are used in the calculations (Genoni *et al.*, 2017). This is mainly due to two simultaneous factors when we use theoretically generated X-ray diffraction data corresponding to a single-molecule/single-atom electron density in a large cubic unit cell (which was the working hypothesis in the considered investigation on correlation effects): (i) the reflections are unevenly distributed in the resolution shells, with the high-angle data far more numerous than the low- and medium-angle ones; (ii) the discrepancies between the structure-factor amplitudes computed at unrestrained level (*i.e.* when $\lambda = 0$) and the corresponding reference values (*i.e.* the structure-factor amplitudes associated with a gas-phase correlated electron density) are quite significant at low and medium angles, while they are generally very small at high angle. Now, bearing in mind the previous two points and considering the expression of $\mathrm{GoF}^2$ [see equation (3)] in the functional to be minimized [see equation (2)], if the high-angle data are fully considered, they predominate and significantly down-weight the contribution of the low- and medium-angle reflections. This was the main reason why the effects of electron correlation on the electron density could be more efficiently and extensively captured only when high-angle data were not employed in the XRW computations.

However, even high-angle reflections contain important information. Therefore, we believe that cutting them off completely is not the best option. To overcome this impasse, we here propose to introduce a weighting factor in the expression of the squared goodness-of-fit, with the goal of increasing the importance of the low- and medium-angle structure-factor amplitudes and, simultaneously, down-weighting the contribution of the high-angle data in a controlled way. In other words, the idea is to modify the expression of $\mathrm{GoF}^2$ as follows:

$$\mathrm{GoF}^2[\Psi_0] = \frac{1}{N_r - N_p}\sum_{\mathbf{h}} w_{\mathbf{h}}\,\frac{\left(\eta\,F_{\mathbf{h}}^{\mathrm{calc}}[\Psi_0] - F_{\mathbf{h}}^{\mathrm{obs}}\right)^2}{\sigma_{\mathbf{h}}^2}, \quad (8)$$

where $w_{\mathbf{h}}$ can be determined by considering the distribution of the reflections in the reciprocal space. In particular, considering a reflection characterized by the Miller indices $\mathbf{h} = (h, k, l)$ and of resolution $\sin\theta_{\mathbf{h}}/\lambda$, we define its weight $w_{\mathbf{h}}$ as the inverse of the 'local density' ($\rho_{\mathbf{h}}$) of X-ray diffraction data at that resolution. Namely, we can write

$$w_{\mathbf{h}} = \frac{1}{\rho_{\mathbf{h}}}, \quad (9)$$

where $\rho_{\mathbf{h}}$ is given by

$$\rho_{\mathbf{h}} = \frac{n_{\mathbf{h}}}{N_r}. \quad (10)$$

In the previous equation, $N_r$ is the total number of X-ray diffraction data considered in the XRW calculation and $n_{\mathbf{h}}$ the number of reflections that fall into the interval $[\sin\theta_{\mathbf{h}}/\lambda - \Delta/2,\ \sin\theta_{\mathbf{h}}/\lambda + \Delta/2]$, with $\Delta$ as an empirical parameter which gives the width of the above-mentioned interval and which can be chosen before starting the computations. As will be described in the next section dedicated to the computational details, in this work we chose different $\Delta$ values to thoroughly assess capabilities and limitations of the proposed weighting scheme.

## 3. Computational details

### 3.1. Theoretical X-ray diffraction data for single atoms/molecules

To start testing the performances of the proposed weighting scheme, we initially performed XRW calculations by using theoretically generated X-ray diffraction data corresponding to the cases of single atoms/molecules in large unit cells. In other words, we worked in the same conditions that were

**Table 1**
XRW calculations with structure-factor amplitudes corresponding to the gas-phase CCSD/UGBS electron density of Ne.

Values of $\lambda_{J,max}$ and of the squared goodness-of-fit in different resolution ranges are given.

| XRW calculation | $\lambda_{J,max}$ | GoF$^2$ Global ($\times10^{-8}$) | Low-angle ($\times10^{-7}$) | Medium-angle ($\times10^{-8}$) | High-angle ($\times10^{-8}$) |
|---|---|---|---|---|---|
| Full data/no weights | 1000.0 | 144.34 | 555.85 | 58.53 | 59.24 |
| No high-angle/no weights | 1000.0 | 159.31 | 315.81 | 118.08 | 108.58 |
| Full data/$\Delta$ = 0.150 Å$^{-1}$ | 100.0 | 16.87 | 24.59 | 9.53 | 15.39 |
| Full data/$\Delta$ = 0.100 Å$^{-1}$ | 100.0 | 7.26 | 9.85 | 3.67 | 7.05 |
| Full data/$\Delta$ = 0.050 Å$^{-1}$ | 100.0 | 1.68 | 2.01 | 0.69 | 1.79 |
| Full data/$\Delta$ = 0.025 Å$^{-1}$ | 99.9 | 0.53 | 0.60 | 0.23 | 0.56 |
| Full data/$\Delta$ = 0.010 Å$^{-1}$ | 100.0 | 0.17 | 0.20 | 0.11 | 0.16 |

**Table 2**
XRW calculations with structure-factor amplitudes corresponding to the gas-phase CCSD/UGBS electron density of HCN.

Values of $\lambda_{J,max}$ and of the squared goodness-of-fit in different resolution ranges are given.

| XRW calculation | $\lambda_{J,max}$ | GoF$^2$ Global ($\times10^{-7}$) | Low-angle ($\times10^{-7}$) | Medium-angle ($\times10^{-8}$) | High-angle ($\times10^{-8}$) |
|---|---|---|---|---|---|
| Full data/no weights | 1000.0 | 38.26 | 794.59 | 514.00 | 137.89 |
| No high-angle/no weights | 1000.0 | 58.20 | 81.13 | 134.11 | 26.79 |
| Full data/$\Delta$ = 0.150 Å$^{-1}$ | 50.0 | 20.73 | 53.15 | 41.46 | 2.87 |
| Full data/$\Delta$ = 0.100 Å$^{-1}$ | 50.0 | 10.87 | 25.99 | 21.49 | 2.10 |
| Full data/$\Delta$ = 0.050 Å$^{-1}$ | 50.0 | 4.15 | 8.28 | 8.87 | 1.23 |
| Full data/$\Delta$ = 0.025 Å$^{-1}$ | 25.2 | 4.10 | 8.04 | 8.41 | 1.30 |
| Full data/$\Delta$ = 0.010 Å$^{-1}$ | 12.5 | 3.35 | 6.87 | 7.04 | 0.95 |

adopted to assess the capabilities of the XRW approach in capturing the effects of electron correlation (Genoni *et al.*, 2017).

In this study we considered the case of the neon (Ne) atom and of hydrogen cyanide (HCN). For each of them, at first, we carried out gas-phase CCSD (coupled cluster with single and double substitutions) calculations with the universal Gaussian basis set (UGBS). Afterwards we performed analytic Fourier transforms of the obtained relaxed CCSD/UGBS electron densities to get the theoretical X-ray structure-factor amplitudes to be used in the following XRW computations. In particular, the theoretical structure factors were generated up to the resolution of 2.0 Å$^{-1}$ and considering only one atom/molecule in a large cubic unit cell with edges of 10 Å (*i.e.* $a = b = c = 10$ Å), for a total of 133 880 reflections in each case. It is worth noting that the use of gas-phase atomic/molecular electron densities allowed us to avoid any intermolecular interaction in the evaluation of the structure factors, while the use of a large unit cell prevented any possible artefact due to the superimposition of neighbouring unit-cell densities. For the sake of completeness, we also mention that the computations of the structure-factor amplitudes were carried out by exploiting an in-house code that uses Obara–Saika recurrence relations for the evaluation of Fourier transform integrals of Gaussian basis function products (Genoni, 2020).

With the theoretically generated structure-factor amplitudes we then carried out XRW calculations (UGBS basis set) adopting different strategies: (i) without applying the weighting scheme and using the full set of available theoretical X-ray diffraction data; (ii) without applying the weighting scheme but neglecting high-angle data [$(\sin\theta/\lambda)_{max}$ equal to 1.44 and 1.00 Å$^{-1}$ for Ne and HCN, respectively]; (iii) applying the weighting scheme described in Section 2.2 with the full set of structure-factor amplitudes. In the last case, five different $\Delta$ values (see Section 2.2) were adopted for the evaluation of the weighting factors: 0.150, 0.100, 0.050, 0.025 and 0.010 Å$^{-1}$.

For Ne, no convergence problems were noticed during the XRW calculations. Therefore, in practically all the situations, we were able to perform the XRW computations until the pre-established maximum values for the $\lambda_J$ parameter: 1000.0 for the calculations without weighting scheme and 100.0 for the computations with weighting scheme (see also Table 1 for all the $\lambda_{J,max}$ values). For HCN, some convergence problems arose when the weighting scheme was applied, especially when the empirical parameter $\Delta$ was small. For this reason, we reduced the maximum $\lambda_J$ value according to the different cases: 1000.0 for the calculations without weighting scheme; 50.0 for the computations with weighting scheme and $\Delta$ equal to 0.150, 0.100 or 0.050 Å$^{-1}$; 25.2 for the calculations with weighting scheme and $\Delta$ equal to 0.025 Å$^{-1}$; and 12.5 for the computations with weighting scheme and $\Delta$ equal to 0.010 Å$^{-1}$ (see also Table 2 for all the $\lambda_{J,max}$ values).

For completeness, in all the above-mentioned XRW calculations with theoretically generated X-ray diffraction data, the standard uncertainties $\sigma_{\mathbf{h}}$ [see equations (3) and (8)] were set equal to 1.0.

### 3.2. Experimental X-ray diffraction data

At a second stage, we decided to apply the proposed weighting scheme also to the case of XRW calculations performed with experimental X-ray diffraction data. To accomplish this task, we used the high-quality and high-resolution data collected by Birkedal *et al.* (2004) for urea [$(\sin\theta/\lambda)_{max}$ = 1.44 Å$^{-1}$]. In this case, we considered all the deposited structure-factor amplitudes except those corresponding to negative intensities, for an overall number of 988 reflections (much lower compared with the situation of the theoretically generated X-ray diffraction data considered above).

The full set of experimental X-ray diffraction data was always used, namely the high-angle reflections were never neglected in the computations. However, also in this case, the XRW calculations (basis set cc-pVTZ) were performed adopting two different options: (i) without the weighting scheme; (ii) with the proposed weighting scheme and using five different values for the empirical parameter $\Delta$: 0.150, 0.100, 0.050, 0.025 and 0.010 Å$^{-1}$.

As already mentioned in Section 2.1, the XRW computations with experimental data for urea were halted at the $\lambda_J$

**Table 3**
XRW calculations with experimental structure-factor amplitudes for urea [$(\sin\theta/\lambda)_{max}$ = 1.44 Å$^{-1}$].

Values of $\lambda_{J,max}$ and of the squared goodness-of-fit in different resolution ranges are given.

| XRW calculation | $\lambda_{J,max}$ ($\times10^{-2}$) | GoF$^2$ Global | Low-angle | Medium-angle | High-angle |
|---|---|---|---|---|---|
| Full data/no weights | 12.5000 | 1.85 | 3.71 | 1.99 | 1.47 |
| Full data/$\Delta$ = 0.150 Å$^{-1}$ | 0.3367 | 2.34 | 2.92 | 3.08 | 1.86 |
| Full data/$\Delta$ = 0.100 Å$^{-1}$ | 0.1977 | 2.40 | 3.02 | 3.20 | 1.89 |
| Full data/$\Delta$ = 0.050 Å$^{-1}$ | 0.1013 | 2.39 | 2.98 | 3.19 | 1.89 |
| Full data/$\Delta$ = 0.025 Å$^{-1}$ | 0.0608 | 2.33 | 2.91 | 3.06 | 1.86 |
| Full data/$\Delta$ = 0.010 Å$^{-1}$ | 0.0344 | 2.18 | 2.78 | 2.76 | 1.79 |

values for which the SCF procedure stopped converging. The actual maximum values of $\lambda_J$ in the different cases can be found in Table 3.

### 3.3. X-ray diffraction data from periodic *ab initio* calculations

As a continuation of the above-described XRW computations with experimental X-ray diffraction data, we afterwards carried out XRW calculations exploiting structure-factor amplitudes resulting from a periodic, single-point (*i.e.* with fixed geometry and fixed unit-cell parameters) DFT-B3LYP computation for urea (basis set cc-pVTZ). In particular, for this periodic calculation, we used the experimental crystal structure deposited by Birkedal *et al.* (2004), namely the crystal structure compatible with the above-considered experimental X-ray data.

We generated two sets of structure-factor amplitudes associated with the obtained periodic B3LYP/cc-pVTZ electron density. At first, we took into account a data set with maximum resolution of 1.44 Å$^{-1}$ (988 reflections) and corresponding to the above-considered set of experimental reflections. This allowed us to better investigate to what extent the performances of the proposed weighting scheme change depending on the use of experimental or theoretical structure-factor amplitudes in the XRW computations when the same number of reflections is used. Afterwards, we considered a larger data set with maximum resolution of 2.00 Å$^{-1}$ (2828 reflections). This enabled us to study the influence of the overall number of reflections (and, consequently, the influence of the maximum resolution) on the capabilities of the strategy introduced in this work.

As for the case with experimental data, in this situation the high-angle reflections were never discarded and the XRW computations (basis set cc-pVTZ) were carried out both with and without the proposed weighting scheme. When the weighting scheme was adopted, we employed the same $\Delta$ values that we used in the two cases described above (namely, 0.150, 0.100, 0.050, 0.025 and 0.010 Å$^{-1}$).

Also for the XRW computations performed with X-ray diffraction data obtained through periodic *ab initio* calculations, the standard uncertainties $\sigma_{\mathbf{h}}$ [see again equations (3) and (8)] were set equal to 1.0 and we halted the procedures when the SCF cycles stopped converging. See Tables 5 and 6 for the maximum values of $\lambda_J$ in the different situations.

### 3.4. Software used

All the gas-phase *ab initio* computations were performed through the *Gaussian09* quantum chemistry package (Frisch *et al.*, 2009), with the corresponding structure-factor amplitudes obtained by means of an in-house code for the evaluation of Fourier transform integrals of basis function products (Genoni, 2020). The *ab initio* periodic calculation and the relative computations of structure-factor amplitudes were carried out by exploiting the software *CRYSTAL14* (Dovesi, Orlando *et al.*, 2014; Dovesi, Saunders *et al.*, 2014). For all the XRW calculations, we used an in-house-modified version of *Gaussian09*, where we implemented the working equations of the XRW approach (see Section 2), including those related to the weighting scheme proposed in this work.

## 4. Results and discussion

In this section, we will discuss the results obtained through the different types of XRW calculations that were described in Section 3. In all considered cases (namely, XRW computations with theoretical gas-phase, experimental or theoretical periodic X-ray diffraction data), the capabilities of the proposed weighting scheme will be assessed by considering not only the global squared goodness-of-fit, but also partial GoF$^2$ values computed by taking into account only specific subsets of the structure-factor amplitudes exploited in the XRW calculations.

### 4.1. XRW calculations with theoretical X-ray diffraction data for Ne

In this subsection, we will analyse the outcomes of the XRW computations that exploited X-ray structure-factor amplitudes associated with the gas-phase CCSD/UGBS electron density of Ne. A general overview of the results can be found in Table 1, where, for all variants of XRW calculations that were performed, we reported both $\lambda_{J,max}$ and the final values of the squared goodness-of-fit associated with the considered resolution ranges. In fact, as mentioned above, in addition to the global GoF$^2$ obtained by considering all the structure-factor amplitudes used in the calculations (namely, in this case, those with $\sin\theta/\lambda \leq 2.0$ Å$^{-1}$), we also determined the squared goodness-of-fit for low-angle ($\sin\theta/\lambda < 0.5$ Å$^{-1}$), medium-angle (0.5 Å$^{-1}$ $\leq \sin\theta/\lambda <$ 1.44 Å$^{-1}$) and high-angle data (1.44 Å$^{-1}$ $\leq \sin\theta/\lambda \leq$ 2.0 Å$^{-1}$).

First, let us focus on the global GoF$^2$ value. In Table 1, we can observe a better fitting of the data (lower GoF$^2$ values) when the proposed weighting scheme is used in the computations. This is also evident in Fig. 1(*a*), where the global squared goodness-of-fit is plotted as a function of the external parameter $\lambda_J$ and where it is possible to note that convergence is achieved (namely, a sort of *plateau* is observed) at smaller $\lambda_J$ values when the weighting scheme is exploited. From the

global $GoF^2$ values reported in Table 1 we can even observe that the weighting scheme allowed us to better reproduce the reference X-ray diffraction data when we assigned smaller values to the empirical parameter $\Delta$ (see Section 2.2). This is confirmed by the inset of Fig. 1(*a*), which also shows that convergence is faster (*i.e.* a plateau is achieved at lower values of $\lambda_J$) when $\Delta$ is smaller.

The better fitting of the X-ray data used as restraints and the faster convergence when the weighting scheme is used can also be observed in Fig. 2, where we have graphically depicted how the differences between calculated and reference structure-factor amplitudes change as we increase $\lambda_J$ in the different situations. In fact, when the full set of data is used without the weighting scheme [Fig. 2(*a*)] or when the high-angle data are simply discarded [Fig. 2(*b*)], it is possible to see that the discrepancies between computed and reference structure-factor amplitudes remain quite high even for very large values of $\lambda_J$. In contrast, when the weighting scheme is introduced [Figs. 2(*c*)–2(*g*)], the absolute deviations tend to flatten, and do so even more rapidly when smaller $\Delta$ values are used in the computations. Related to this last point, it is worth noting that, as $\Delta$ becomes smaller and smaller, it is as a specific weight was assigned to each reflection. In other words, as $\Delta \rightarrow 0$, each reflection tends to have its own $\lambda_J$ value [remember that the general and external $\lambda_J$ parameter multiplies $GoF^2$ in the expression of functional $J$ given by equation (2)]. Therefore, in those circumstances, it is as though we were almost really performing X-ray 'constrained' wavefunction computations. This is confirmed by the fact that, when we employ smaller values of $\Delta$ in the weighting scheme, we increase our capability of exactly reproducing the reference structure-factor amplitudes [see again Figs. 2(*c*)–2(*g*)].

Finally, to complete our discussion about the global squared goodness-of-fit, from Fig. 1(*a*) we can also see that the neglect of high-angle data is not a recommended solution because, starting from a certain value of the external parameter $\lambda_J$, global $GoF^2$ starts increasing, thus indicating a worse fitting of the reference data. This can also be evinced by analysing Fig. 2(*b*). In fact, it is easy to see that, when we increase $\lambda_J$, the fitting of the low-angle data improves, while the medium/high-angle description worsens. This will be further discussed below, when the specific squared goodness-of-fit for medium- and high-angle X-ray data will be considered and analysed in detail.

From this point on, we will analyse $GoF^2$ for specific subsets of the X-ray diffraction data. Let us start with the low-angle region. Also in this case, we have better fittings (*i.e.* lower $GoF^2$ values; Table 1) and faster convergence [*i.e.* a plateau at smaller values of $\lambda_J$; Fig. 1(*b*)] when the weighting scheme is adopted. Moreover, the agreement with the reference data

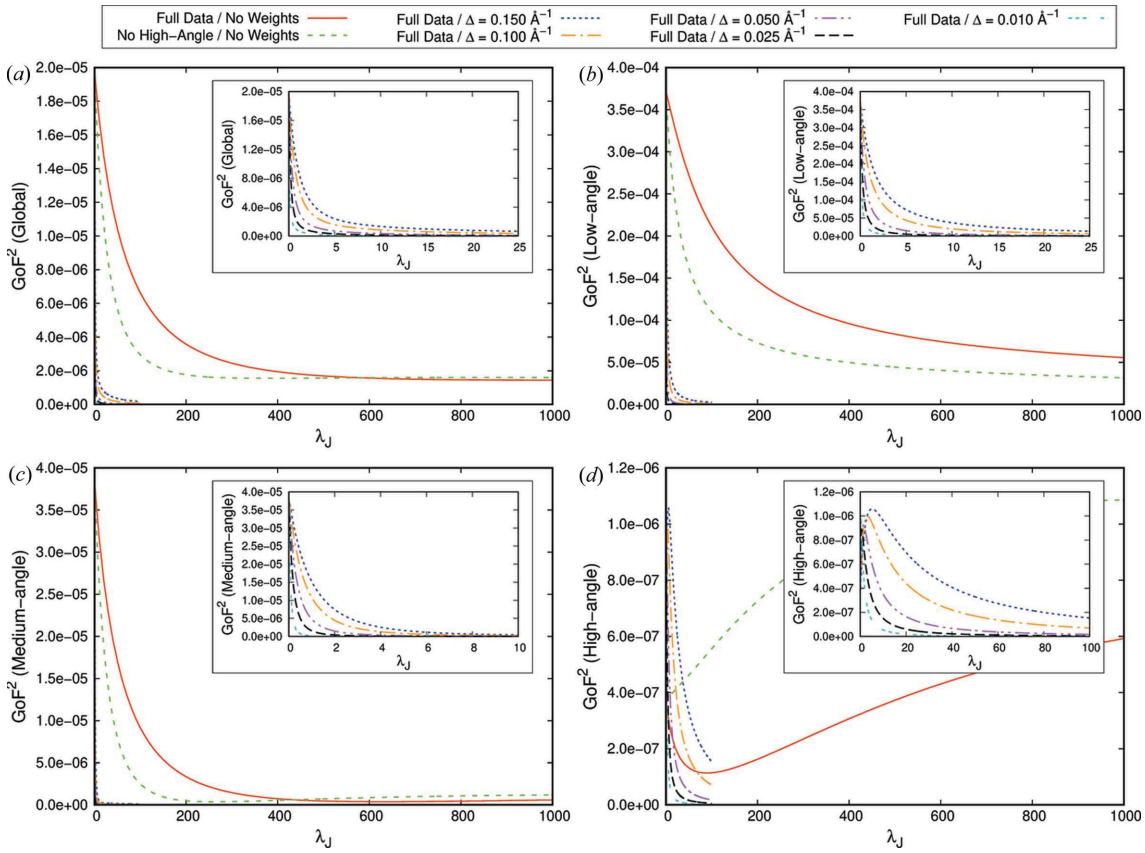


**Figure 1**
$GoF^2$ as a function of $\lambda_J$ in different resolution ranges for the XRW calculations performed with structure-factor amplitudes corresponding to the gas-phase CCSD/UGBS electron density of Ne: (*a*) global $GoF^2$, (*b*) low-angle $GoF^2$, (*c*) medium-angle $GoF^2$ and (*d*) high-angle $GoF^2$. The insets show the magnified plots only for the XRW calculations carried out with the weighting scheme.

and the 'rate of convergence' improves as the parameter Δ becomes smaller and smaller [see again Table 1 and the inset of Fig. 1(*b*)]. Analysing Fig. 1(*b*), we can also observe that the fitting of the low-angle data is almost impossible or extremely slow when the full set of X-ray data is exploited without the weighting scheme. At the same time, the neglect of the high-

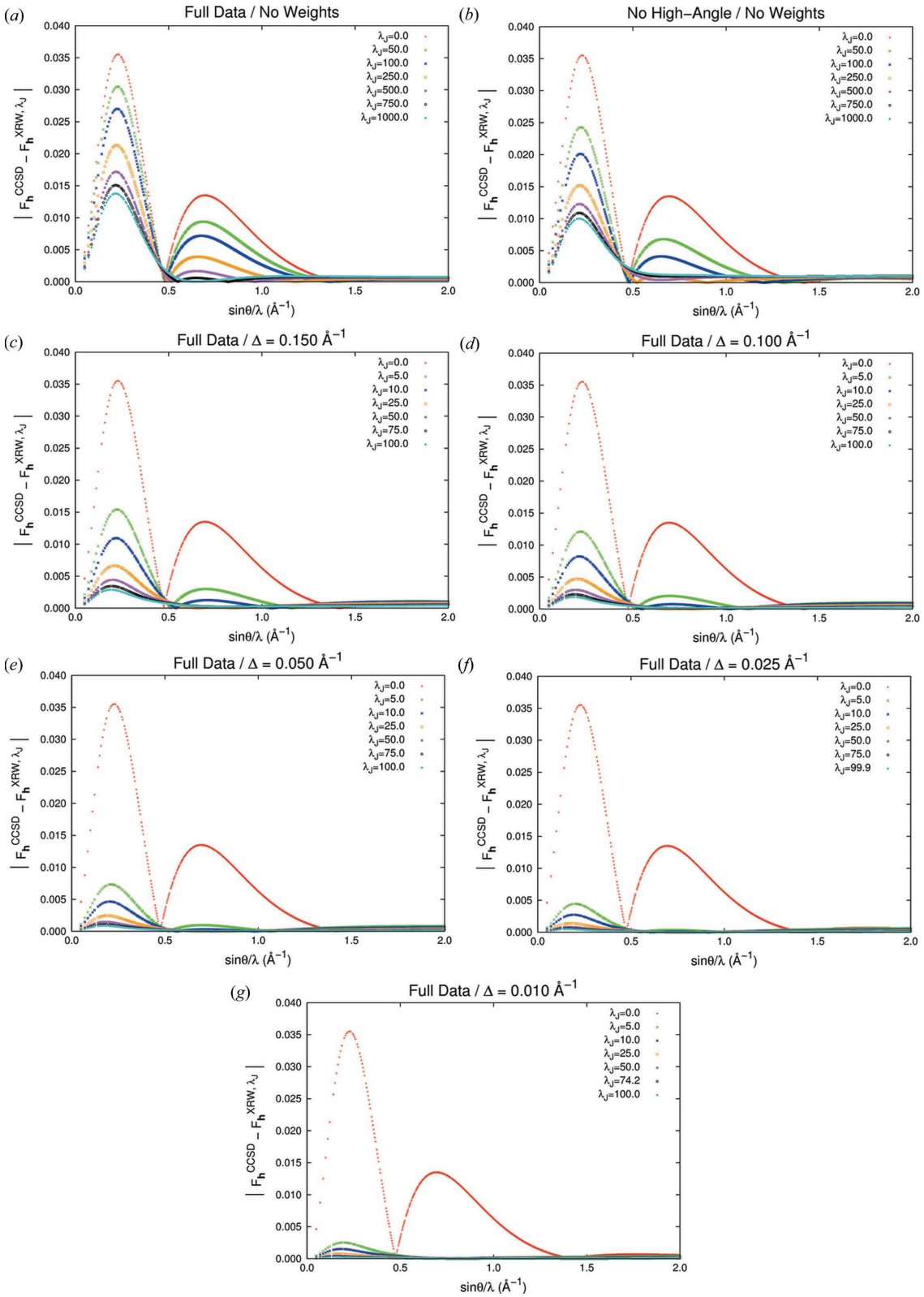


**Figure 2**
Absolute differences between calculated and reference structure-factor amplitudes at different values of $\lambda_J$ for XRW calculations performed with X-ray diffraction data corresponding to the gas-phase CCSD/UGBS electron density of Ne: (*a*) full set of data without weighting scheme, (*b*) no high-angle data without weighting scheme, (*c*)–(*e*) full set of data with weighting scheme and different values of the Δ parameter.

angle reflections in the computations allows us to speed up convergence, but not in a decisive way and, above all, this approach leads to a worse description of the high-angle region. This can be seen by considering Figs. 2(*a*) and 2(*b*). Although the neglect of high-angle data allows us to better fit the low-angle structure-factor amplitudes when the same $\lambda_J$ values are used [compare the corresponding low-angle peaks in Figs. 2(*a*) and 2(*b*)], it worsens the description of the medium- and high-angle data [compare again Figs. 2(*a*) and 2(*b*), but in the medium- and high-angle regions].

Now, let us consider the results obtained for the medium-angle subset of X-ray diffraction data. As observed in the low-angle case, we have a better fitting of the reference structure-factor amplitudes and a faster convergence when the weighting scheme is applied [see Table 1 and Fig. 1(*c*)]. Once again, the reproduction of the reference X-ray data and convergence improve when the parameter $\Delta$ of the weighting scheme decreases [see again Table 1 and the inset of Fig. 1(*c*)]. By inspecting Fig. 1(*c*), it is also interesting to notice that, when the weighting scheme is not adopted, not only do we have a slower convergence, but, for large values of $\lambda_J$, the description of the medium-angle data worsens, namely $GoF^2$ increases. This occurs both when the full set of data is used in the computations and when the high-angle reflections are discarded. The latter case is even more evident. All the trends that we have just described also correlate quite well with the absolute deviations between XRW and reference structure-factor amplitudes in the medium-angle region reported in Fig. 2.

To conclude the analysis of the results obtained for Ne, we will now focus on the squared goodness-of-fit for the high-angle region. In this case, when the full set of X-ray data is used without the weighting scheme, $GoF^2$ initially decreases but it afterwards increases as a function of $\lambda_J$ [see Fig. 1(*d*)]. An even worse behaviour is observed for the XRW computations performed without considering the high-angle reflections (and without the weighting scheme). In fact, since the high-angle data are completely neglected, their description/fitting worsens as a function of $\lambda_J$ [see again Fig. 1(*d*)]. In contrast, the descriptions improve when the complete set of structure-factor amplitudes is exploited along with the proposed weighting scheme: for all the considered $\Delta$ values, $GoF^2$ initially increases (for small values of $\lambda_J$) and then it monotonically decreases as a function of $\lambda_J$ [see the inset of Fig. 1(*d*)]. In particular, the decrease is faster when $\Delta$ is smaller [see Fig. 1(*d*) and its inset]. As for the low- and medium-angle regions, in this case, the observed trends correlate with the absolute discrepancies of the structure-factor amplitudes shown in Fig. 2.

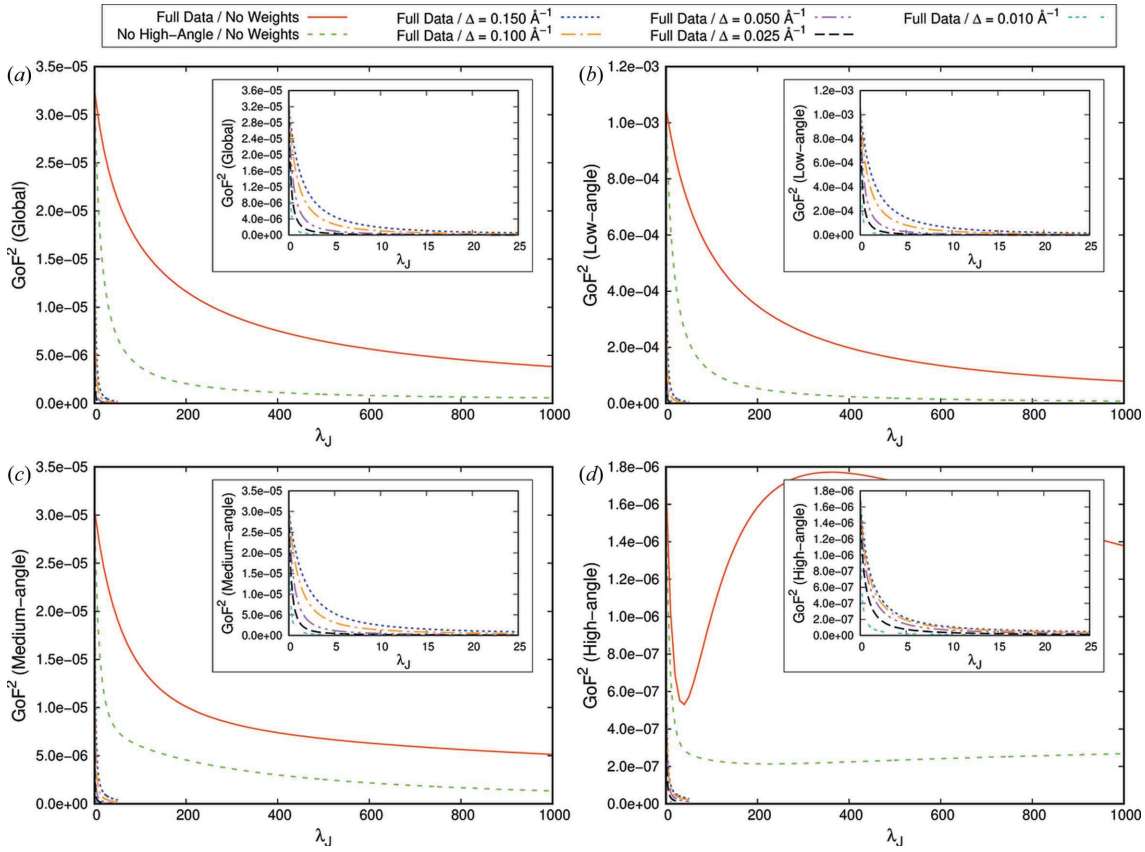


**Figure 3**
$GoF^2$ as a function of $\lambda_J$ in different resolution ranges for the XRW calculations performed with structure-factor amplitudes corresponding to the gas-phase CCSD/UGBS electron density of HCN: (*a*) global $GoF^2$, (*b*) low-angle $GoF^2$, (*c*) medium-angle $GoF^2$ and (*d*) high-angle $GoF^2$. The insets show the magnified plots only for the XRW calculations carried out with the weighting scheme.

### 4.2. XRW calculations with theoretical X-ray diffraction data for HCN

This subsection will focus on the results of the XRW calculations with X-ray structure-factor amplitudes corresponding to the gas-phase CCSD/UGBS electron density of hydrogen cyanide. As for Ne, in addition to the global squared goodness-of-fit, we also analysed the $GoF^2$ values related to specific subsets of reflections: low-angle (in this case, $\sin\theta/\lambda < 0.6$ Å$^{-1}$), medium-angle ($0.6$ Å$^{-1} \leq \sin\theta/\lambda < 1.0$ Å$^{-1}$) and high-angle ($1.0$ Å$^{-1} \leq \sin\theta/\lambda \leq 2.0$ Å$^{-1}$) data.

Let us consider the global case. In Table 2 and Fig. 3(*a*), we can observe a better fitting of the reference structure-factor amplitudes (*i.e.* lower $GoF^2$ values) and faster convergence (*i.e.* a plateau at lower $\lambda_J$ values) when the weighting scheme is applied. Moreover, as for Ne, description and convergence improve by decreasing the value of the empirical parameter $\Delta$ [see again Table 2 and the inset of Fig. 3(*a*)]. These trends find correspondence in the figures reporting the absolute differences between the XRW and reference CCSD/UGBS structure-factor amplitudes at different values of $\lambda_J$ for the different types of XRW computations that were performed (see Figs. S1–S7 in the supporting information). Finally, by inspecting Fig. 3(*a*), we can also observe that, if the high-angle data are not used, the global description improves, and convergence increases compared with the case in which the full set of structure-factor amplitudes is exploited without the weighting scheme. However, this improvement is not a decisive one, at least not as decisive as when the full set of reflections is employed along with weights [see again Fig. 3(*a*)]. Furthermore, as will be discussed below in detail, also for HCN, the neglect of the high-angle data inevitably leads to worse descriptions in the high-angle region.

Concerning the squared goodness-of-fit for the low- and medium-angle reflections, similar trends have been observed. They are somehow similar to those outlined above for global $GoF^2$. In fact, also in these situations, we observe better fittings of the data (lower $GoF^2$ values; see Table 2) and faster convergence [a plateau at lower values of $\lambda_J$; see Figs. 3(*b*) and 3(*c*)] when the full set of structure-factor amplitudes is employed together with the weighting scheme. Furthermore, as in the global case, the neglect of the high-angle data helps in better fitting the low- and medium-angle data, but not as efficiently as when the weights of the reflections are introduced in the XRW calculations [see again Table 2 and Figs. 3(*b*) and 3(*c*)]. Finally, in Table 2 and in the insets of Figs. 3(*b*) and 3(*c*), we can clearly notice that the fitting improves, and convergence is faster when the $\Delta$ parameter of the proposed weighting scheme becomes smaller.

Now, let us focus on the results obtained for the high-angle region. When all the reflections are used without weights, we

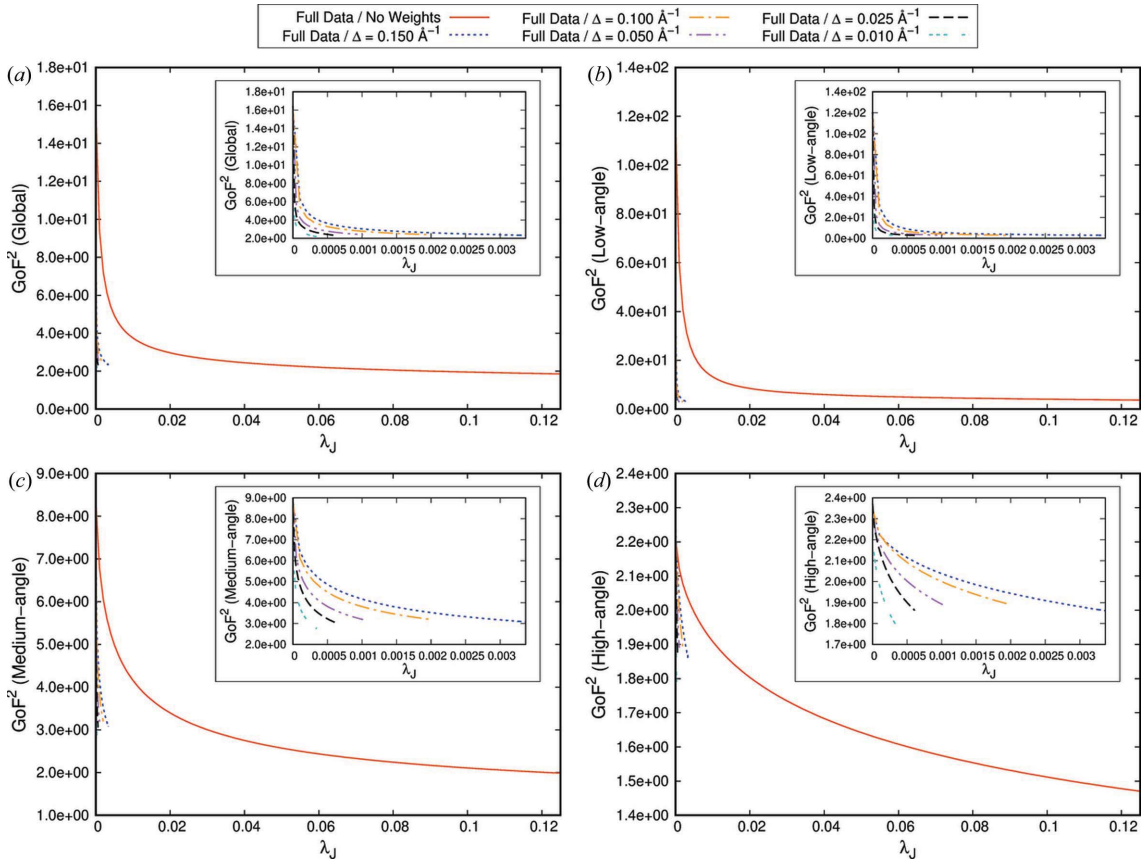


**Figure 4**
$GoF^2$ as a function of $\lambda_J$ in different resolution ranges for the XRW calculations performed with experimental structure-factor amplitudes for urea: (*a*) global $GoF^2$, (*b*) low-angle $GoF^2$, (*c*) medium-angle $GoF^2$ and (*d*) high-angle $GoF^2$. The insets show the magnified plots only for the XRW calculations carried out with the weighting scheme.

observe an erratic trend of the squared goodness-of-fit as a function of $\lambda_J$ [see Fig. 3(*d*)]. In fact, GoF$^2$ initially decreases, then it increases and, after reaching a maximum, it decreases again. This erratic behaviour is not observed when the high-angle data are simply discarded without application of the weighting scheme. However, in that case, although GoF$^2$ initially decreases, it starts increasing at a certain value of $\lambda_J$ [see again Fig. 3(*d*)], thus indicating again that the simple neglect of high-angle data is not a recommended solution. In contrast, when the full set of structure-factor amplitudes is used with weights, we obtain a better reproduction of the high-angle reference data (see Table 2), in addition to a faster convergence and a monotonically decreasing trend of GoF$^2$ as a function of $\lambda_J$ [see Fig. 3(*d*) and its inset]. Moreover, as for the low- and medium-angle regions, for the high-angle data convergence improves when the weighting scheme is applied with smaller values of the parameter $\Delta$ [see the inset of Fig. 3(*d*)].

### 4.3. XRW calculations with experimental X-ray diffraction data for urea

The two test cases discussed above have confirmed that, when the full set of gas-phase theoretically generated structure-factor amplitudes is used in XRW computations without the weighting scheme, it is not possible to fully capture the information contained in the low-angle reflections. The results have also shown that neglect of the high-angle data [a possibility that was proposed in the investigation on electron correlation effects (Genoni *et al.*, 2017)] is not an efficient and definitive solution to the problem either. In fact, it improves the description in the low-angle region but not in a definitive way and, above all, it leads to worse results at medium and high angles. However, the application of the proposed weighting scheme leads to more balanced results and enables better reproductions of the reference structure-factor amplitudes with faster convergence, not only in the global case but also for the different resolution ranges that were considered.

However, the previous results referred only to theoretical X-ray diffraction data corresponding to single-atom/molecule electron densities in large unit cells. To prove the general applicability of the introduced weighting scheme, in this subsection we will discuss the more realistic case in which experimental structure-factor amplitudes are used as restraints. This analysis is also fundamental to critically evaluating the possibility of performing XRW computations with multiple adjustable parameters $\lambda_J$ (namely, different $\lambda_J$ parameters for the low-, medium- and high-angle resolution regions), as recently envisaged by Landeros-Rivera *et al.* (2021).

Below we will analyse the outcomes of XRW calculations carried out with experimental X-ray structure-factor amplitudes collected by Birkedal *et al.* (2004) for the urea crystal up to a maximum resolution of 1.44 Å$^{-1}$. As for the case of the theoretically generated X-ray data, we did not consider just the global squared goodness-of-fit, but also GoF$^2$ values corresponding to different resolution ranges, particularly

**Table 4**
Number of reflections (in brackets the percentage) and average absolute discrepancies between reference and unrestrained ($\lambda_J$ = 0) structure-factor amplitudes (in brackets the ratio with respect to the low-angle value) in different regions of the reciprocal space for different types of X-ray diffraction data used as restraints in the XRW computations.

Low-angle: $\sin\theta/\lambda \leq 0.6$ Å$^{-1}$; medium-angle: 0.6 Å$^{-1}$ < $\sin\theta/\lambda \leq 1.0$ Å$^{-1}$; high-angle: $\sin\theta/\lambda > 1.0$ Å$^{-1}$.

| | No. of reflections | $\langle\lvert F_{\mathbf{h}}^{\rm obs} - F_{\mathbf{h}}^{\rm XRW,\,\lambda_J=0}\rvert\rangle$† |
|---|---|---|
| HCN (gas-phase CCSD/UGBS 2.0 Å$^{-1}$) | | |
| Low-angle | 3564 (2.7%) | $2.42 \times 10^{-2}$ (1.00) |
| Medium-angle | 13130 (9.8%) | $4.42 \times 10^{-3}$ (0.29) |
| High-angle | 117186 (87.5%) | $5.87 \times 10^{-4}$ (0.04) |
| Urea (experimental 1.44 Å$^{-1}$) | | |
| Low-angle | 101 (10.2%) | $2.85 \times 10^{-1}$ (1.00) |
| Medium-angle | 298 (30.2%) | $1.05 \times 10^{-1}$ (0.38) |
| High-angle | 589 (59.6%) | $1.02 \times 10^{-1}$ (0.37) |
| Urea (periodic B3LYP/cc-pVTZ 1.44 Å$^{-1}$) | | |
| Low-angle | 101 (10.2%) | $9.00 \times 10^{-2}$ (1.00) |
| Medium-angle | 298 (30.2%) | $1.81 \times 10^{-2}$ (0.20) |
| High-angle | 589 (59.6%) | $1.20 \times 10^{-2}$ (0.13) |
| Urea (periodic B3LYP/cc-pVTZ 2.0 Å$^{-1}$) | | |
| Low-angle | 101 (3.6%) | $9.00 \times 10^{-2}$ (1.00) |
| Medium-angle | 302 (10.7%) | $1.81 \times 10^{-2}$ (0.20) |
| High-angle | 2425 (85.7%) | $8.30 \times 10^{-3}$ (0.09) |

† The unrestrained structure-factor amplitudes ($F_{\mathbf{h}}^{\rm XRW,\,\lambda_J=0}$) are properly scaled in the case of experimental data for urea.

GoF$^2$ values related to the low-angle ($\sin\theta/\lambda < 0.6$ Å$^{-1}$), medium-angle (0.6 Å$^{-1}$ $\leq \sin\theta/\lambda <$ 1.0 Å$^{-1}$) and high-angle (1.0 Å$^{-1}$ $\leq \sin\theta/\lambda \leq$ 1.44 Å$^{-1}$) regions.

Let us start analysing the results obtained for the global squared goodness-of-fit. First, by inspecting Fig. 4(*a*), we can notice that, unlike the above-discussed cases of theoretical X-ray diffraction data, convergence problems arose (*i.e.* the SCF computations stopped converging) when the weighting scheme was adopted. This is independent of the chosen value for the parameter $\Delta$. Moreover, the traditional XRW computation with the full set of data and without weights for the reflections provided a final value of global GoF$^2$ that is lower than the final GoF$^2$ values resulting from the XRW computations performed with the weighting scheme (see Table 3). The convergence problems are also clearly visible in the inset of Fig. 4(*a*), where a plateau is not really reached regardless of the value of the parameter $\Delta$ chosen to define the weights of the reflections.

A possible explanation for the obtained results can be found by considering the fact that the high-angle reflections are not sufficiently considered in the calculations with the weighting scheme because using real experimental X-ray diffraction data in XRW computations is not identical to exploiting theoretically generated X-ray structure-factor amplitudes for a single atom/molecule in a large unit cell. In fact, as can be observed in Table 4 and Fig. S8A in the supporting information, in the experimental situation, (i) the high-angle reflections are not numerically dominant as in the purely theoretical case of Ne and HCN (see the second

column of Table 4), and (ii) when $\lambda_J = 0$, the discrepancies between calculated and experimental structure-factor amplitudes at high angle are not significantly lower than the discrepancies observed at low and medium angle, but, in contrast, they are of the same order of magnitude (see the third column of Table 4). Therefore, down-weighting the high-angle data might introduce some problems when real experimental reflections are used. It seems that some important information in the high-angle range would be left out and not properly considered in the XRW computations. This will also be confirmed by the results discussed below for the medium- and high-angle regions.

We will now focus on the squared goodness-of-fit for the low-angle structure-factor amplitudes. In Table 3 and Fig. 4(*b*) we can observe that the use of the weighting scheme indeed allowed a better fitting of the low-angle data. Furthermore, the inset of Fig. 4(*b*) shows that a sort of convergence is almost reached when the structure-factor amplitudes are weighted according to the method proposed in Section 2.2. These results indicate that, when the weighting scheme was exploited, it was possible to better reproduce the low-angle reflections because, in those situations, the low-angle data had larger weights in the functional to be minimized.

Concerning the results obtained in the medium- and high-angle regions, we can notice that convergence is never practically reached (*i.e.* a plateau is never observed) when the reflection weights are introduced in the XRW calculations [see Figs. 4(*c*)–4(*d*) and their insets]. Moreover, the final medium- and high-angle $GoF^2$ values obtained with the weighting scheme are always larger than that resulting from the corresponding traditional XRW computation without weights (see Table 3). These outcomes further confirm that, in the case of XRW calculations with experimental X-ray diffraction data for urea, the proposed weighting scheme was useful to give more importance to and to better fit the low-angle structure-factor amplitudes. Nevertheless, this was not a suitable strategy to properly account for the information contained in the medium- and high-angle reflections.

Therefore, the results analysed so far show that the weighting scheme works quite well when one uses theoretically generated X-ray data associated with single-atom/molecule electron densities in large unit cells, while the proposed approach is less efficient when experimental structure-factor amplitudes are exploited. This also consequently indicates that the use of different $\lambda_J$ parameters for different resolution ranges might not be an ideal solution when experimental reflections are employed in XRW calculations. However, to complete our analysis and to draw more solid conclusions, in the next subsection we will also discuss the results obtained from XRW computations (with and without the weighting

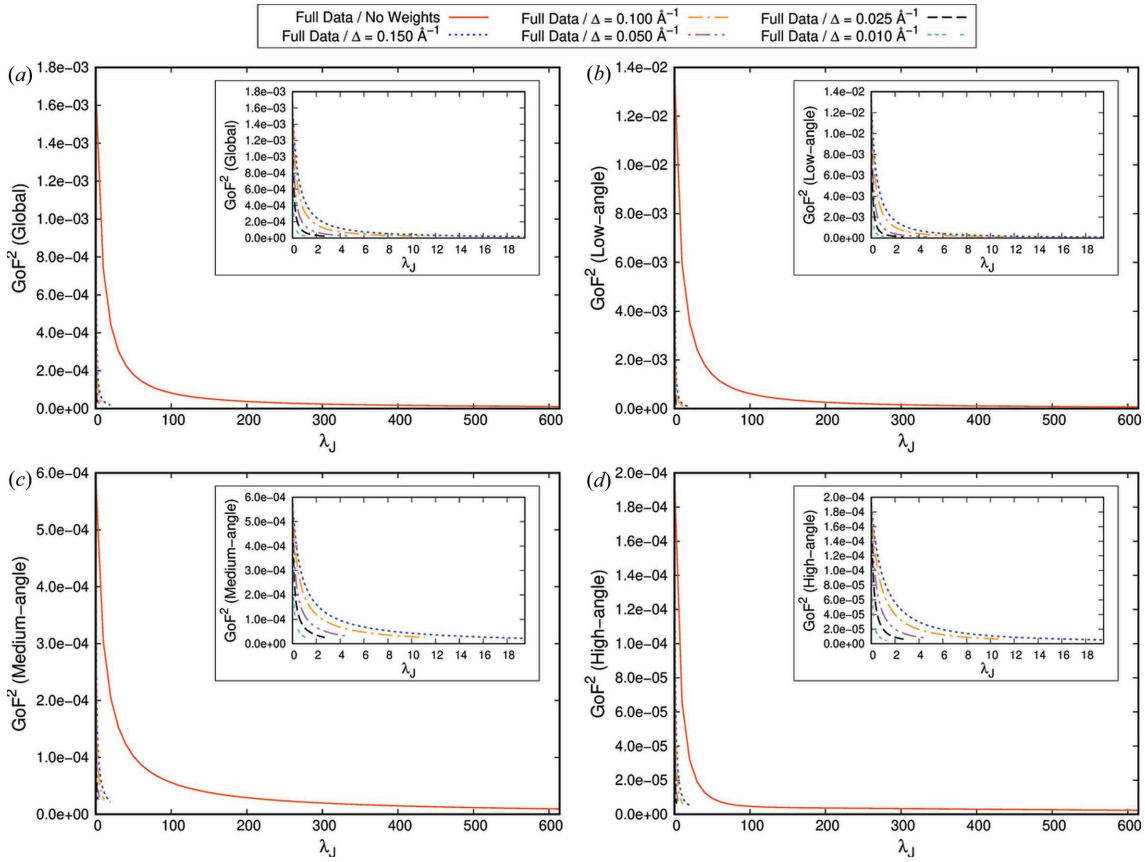


**Figure 5**
$GoF^2$ as a function of $\lambda_J$ in different resolution ranges for the XRW calculations performed with structure-factor amplitudes corresponding to the periodic B3LYP/cc-pVTZ electron density of urea [$(\sin\theta/\lambda)_{max} = 1.44$ Å$^{-1}$]: (*a*) global $GoF^2$, (*b*) low-angle $GoF^2$, (*c*) medium-angle $GoF^2$ and (*d*) high-angle $GoF^2$. The insets show the magnified plots only for the XRW calculations carried out with the weighting scheme.

scheme) when X-ray diffraction data resulting from *ab initio* periodic computations were used as restraints.

### 4.4. XRW calculations with periodic *ab initio* X-ray diffraction data for urea

To complete the assessment of the weighting scheme, in this subsection we will analyse the results of XRW computations performed with X-ray structure-factor amplitudes resulting from preliminary single-point DFT-B3LYP periodic calculations on the experimental crystal structure of urea. As already indicated in the section dedicated to computational details, two cases were analysed: in one we considered the same maximum resolution as in the experimental case (*i.e.* 1.44 Å$^{-1}$ for a total amount of 988 data used as restraints), while in the other one the maximum resolution was set to 2.0 Å$^{-1}$ (for an overall amount of 2828 reflections). As in the previous analyses, in both situations we did not consider just the global squared goodness-of-fit, but also the GoF$^2$ values corresponding to specific resolution ranges (low-angle: $\sin\theta/\lambda < 0.6$ Å$^{-1}$; medium-angle: 0.6 Å$^{-1} \leq \sin\theta/\lambda < 1.0$ Å$^{-1}$; and high-angle: 1.0 Å$^{-1} \leq \sin\theta/\lambda \leq 1.44$ Å$^{-1}$ or 1.0 Å$^{-1} \leq \sin\theta/\lambda \leq 2.0$ Å$^{-1}$).

First of all, let us discuss the results of the XRW computations with X-ray diffraction data having maximum resolution of 1.44 Å$^{-1}$, and let us particularly focus on the global squared goodness-of-fit. Fig. 5(*a*) shows that, independently of the adopted Δ value, we run into convergence problems when the full set of reflections was used along with the weighting scheme. In fact, in all these cases, a plateau is never distinctly reached in the plots of global GoF$^2$ as a function of $\lambda_J$. Furthermore, in Table 5, we can also see that the XRW calculations with the weighting scheme provided final values for the global squared goodness-of-fit that are larger than that resulting from the corresponding traditional XRW computation without weights.

The explanation of the above-reported results could be found again in the improper weight assigned to the medium- and high-angle data, which are not significantly much more numerous compared with the low-angle ones. This can be seen in Fig. S8B in the supporting information and, above all, in Table 4 by comparing the percentages of reflections in the different resolution regions for this case [*i.e.* urea periodic B3LYP (1.44 Å$^{-1}$)] with those observed in the case of theoretically generated X-ray data associated with the gas-phase electron density of HCN. Moreover, although the discrepancies between unrestrained ($\lambda_J = 0$) and reference structure-factor amplitudes at medium/high angle are lower than those observed at low angle (see the third column of Table 4), they are not as low as those observed in the case of theoretically generated structure-factor amplitudes for gas-phase-like molecules (especially for the high-angle reflections).

Finally, concerning the three different resolution regions, we obtained similar trends, with convergence that is never reached clearly when the weights are introduced. In fact, a plateau cannot be distinctly noticed in the different GoF$^2$ vs $\lambda_J$ graphs, especially for the medium- and high-angle regions [see Figs. 5(*b*), 5(*c*), 5(*d*) and their insets]. Moreover, in all cases, the final GoF$^2$ values obtained with the weighting scheme are larger than those obtained by using the full set of X-ray data without weights.

**Table 5**
XRW calculations with structure-factor amplitudes corresponding to the periodic B3LYP/cc-pVTZ electron density of urea [$(\sin\theta/\lambda)_{max}$ = 1.44 Å$^{-1}$].

Values of $\lambda_{J,max}$ and of the squared goodness-of-fit in different resolution ranges are given.

| | | GoF$^2$ | | | |
|---|---|---|---|---|---|
| XRW calculation | $\lambda_{J,max}$ | Global ($\times10^{-5}$) | Low-angle ($\times10^{-5}$) | Medium-angle ($\times10^{-5}$) | High-angle ($\times10^{-6}$) |
| Full data/no weights | 613.99 | 1.11 | 6.70 | 0.94 | 2.36 |
| Full data/Δ = 0.150 Å$^{-1}$ | 19.40 | 1.90 | 8.91 | 2.22 | 5.31 |
| Full data/Δ = 0.100 Å$^{-1}$ | 11.07 | 2.27 | 10.94 | 2.59 | 6.24 |
| Full data/Δ = 0.050 Å$^{-1}$ | 4.67 | 2.68 | 12.79 | 3.04 | 7.72 |
| Full data/Δ = 0.025 Å$^{-1}$ | 2.70 | 2.30 | 11.11 | 2.62 | 6.34 |
| Full data/Δ = 0.010 Å$^{-1}$ | 1.31 | 1.91 | 9.58 | 2.17 | 4.61 |

Let us now consider and analyse the results obtained for the global squared goodness-of-fit when we used X-ray diffraction data with a maximum resolution of 2.0 Å$^{-1}$. Also in this case, we had convergence problems when the reflection weights were exploited [see Fig. 6(*a*)]. However, it is worth noting that, in this situation, the final value of the global GoF$^2$ obtained with the weighting scheme is almost always lower than the one that resulted from the traditional XRW computation without weights (see Table 6), the only exception being when Δ is equal to 0.050 Å$^{-1}$. Furthermore, by comparing Tables 5 and 6, we can observe that, in this case, the $\lambda_{J,max}$ values are systematically larger than those observed for the XRW computations with X-ray data having maximum resolution of 1.44 Å$^{-1}$, thus suggesting that convergence problems are less serious compared with the previous situation.

The previous trends can be explained by considering that we are in a case that is more like the one for theoretically generated X-ray data for gas-phase-like atoms/molecules (as for Ne and HCN discussed above). In fact, the high-angle data start becoming numerically dominant (see the second column in Table 4), and most of the absolute deviations between unrestrained ($\lambda_J = 0$) and calculated structure-factor amplitudes at high angle are quite low (see Fig. S8C in the supporting information). This is also confirmed by the values reported in the third column of Table 4 which clearly indicate how the trend that we have in this situation is closer (although not yet identical) to the one with the theoretically generated X-ray diffraction data for HCN in the gas phase.

To complete the discussion, we now analyse the results obtained for the three different resolution regions. Pertaining to the low-angle one, in Table 6 and Fig. 6(*b*), we can observe that the use of the reflection weights almost always led to better fittings compared with the case in which the full set of reflections is used without weights (the only exception is for Δ = 0.050 Å$^{-1}$). Moreover, the inset of Fig. 6(*b*) also shows

**Table 6**
XRW calculations with structure-factor amplitudes corresponding to the periodic B3LYP/cc-pVTZ electron density of urea [$(\sin\theta/\lambda)_{max}$ = 2.00 Å$^{-1}$].

Values of $\lambda_{J,max}$ and of the squared goodness-of-fit in different resolution ranges are given.

| | | GoF$^2$ | | | |
|---|---|---|---|---|---|
| XRW calculation | $\lambda_{J,max}$ | Global ($\times10^{-6}$) | Low-angle ($\times10^{-5}$) | Medium-angle ($\times10^{-5}$) | High-angle ($\times10^{-6}$) |
| Full data/no weights | 990.00 | 6.91 | 11.35 | 1.39 | 1.60 |
| Full data/$\Delta$ = 0.150 Å$^{-1}$ | 22.00 | 6.49 | 7.70 | 2.00 | 1.88 |
| Full data/$\Delta$ = 0.100 Å$^{-1}$ | 14.24 | 6.62 | 7.94 | 2.03 | 1.88 |
| Full data/$\Delta$ = 0.050 Å$^{-1}$ | 5.05 | 9.26 | 11.86 | 2.89 | 2.26 |
| Full data/$\Delta$ = 0.025 Å$^{-1}$ | 3.92 | 5.84 | 6.81 | 1.80 | 1.73 |
| Full data/$\Delta$ = 0.010 Å$^{-1}$ | 1.83 | 5.34 | 6.16 | 1.56 | 1.73 |

that convergence is almost reached for low-angle data when the proposed weighting scheme is introduced.

Finally, let us consider the medium- and high-angle regions. When the weights are used, the final GoF$^2$ values are always larger than those obtained by using the full set of X-ray data without the weighting scheme (see Table 6). However, compared with the 1.44 Å$^{-1}$ case, the differences between results obtained with or without the weighting scheme are smaller (compare the differences in Tables 5 and 6). This further confirms that, by exploiting periodic B3LYP X-ray structure-factor amplitudes with $(\sin\theta/\lambda)_{max}$ = 2.0 Å$^{-1}$, we are approaching the case of gas-phase theoretically generated X-ray data (see again Table 4).

The results shown in this subsection indicate that, also in the case of XRW computations with X-ray diffraction data generated from periodic *ab initio* calculations, the weighting scheme is not as efficient as when it is applied to X-ray structure-factor amplitudes corresponding to electron densities of single atoms/molecules in large unit cells. However, it was also observed that, by increasing the maximum resolution to 2.0 Å$^{-1}$ (a value larger than the maximum resolution generally attainable in accurate X-ray diffraction measurements for charge-density studies), the performances of the proposed approach improve. This suggests that the weighting scheme might be profitably exploited in those cases in which many X-ray diffraction data are available.

## 5. Conclusions and perspectives

In this work, starting from the results of a previous investigation that aimed to study the capability of the Jayatilaka approach in extracting correlation effects on the electron density (Genoni *et al.*, 2017), we have proposed a weighting scheme for the XRW approach. Mainly based on the concept of reflection distribution in the reciprocal space, the approach

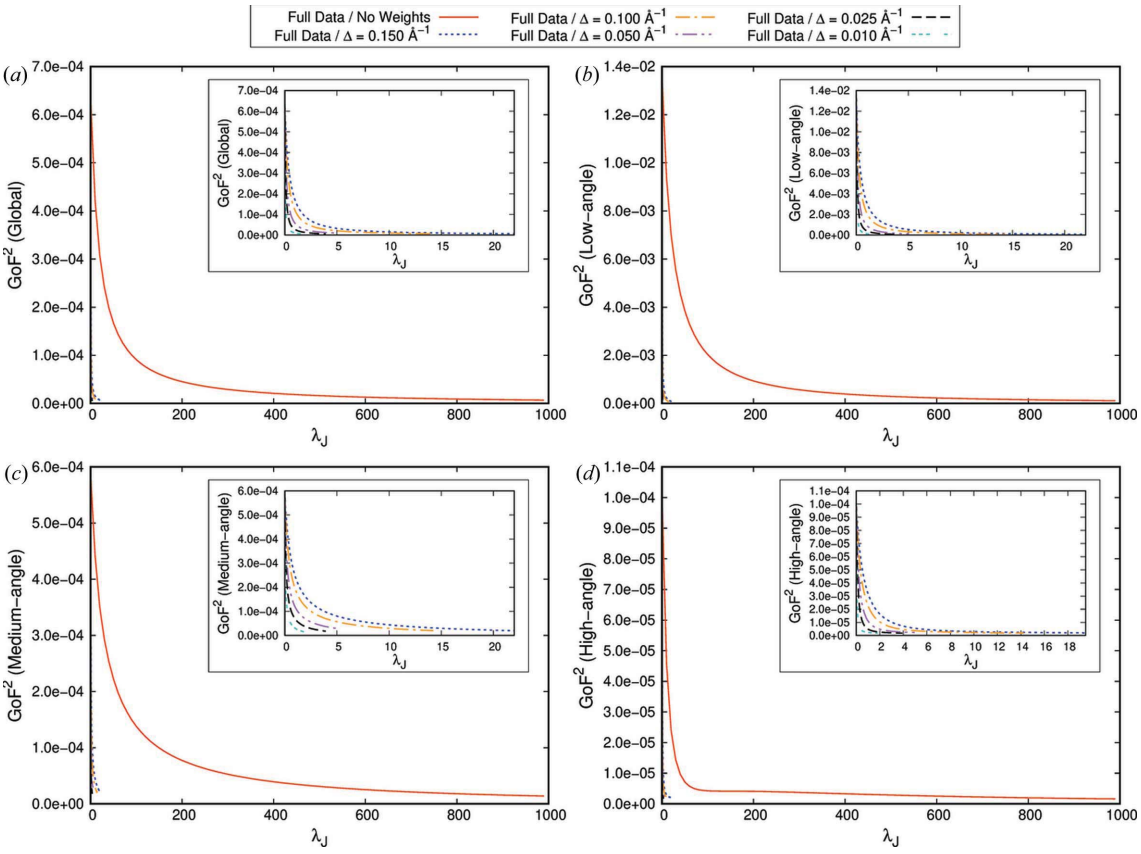


**Figure 6**
GoF$^2$ as a function of $\lambda_J$ in different resolution ranges for the XRW calculations performed with structure-factor amplitudes corresponding to the periodic B3LYP/cc-pVTZ electron density of urea [$(\sin\theta/\lambda)_{max}$ = 2.00 Å$^{-1}$]: (*a*) global GoF$^2$, (*b*) low-angle GoF$^2$, (*c*) medium-angle GoF$^2$ and (*d*) high-angle GoF$^2$. The insets show the magnified plots only for the XRW calculations carried out with the weighting scheme.

has the goal of properly taking into account the contributions of all the available reflections without neglecting a part of them to better capture a property of interest, as was initially suggested in the study on the electron correlation effects. The weighting scheme has been thoroughly tested by considering different types of X-ray diffraction data as restraints in the XRW calculations: (i) structure-factor amplitudes corresponding to highly correlated *ab initio* electron densities of single atoms/molecules in large unit cells, (ii) traditional high-resolution experimental structure-factor amplitudes, and (iii) structure-factor amplitudes associated with electron distributions obtained by means of periodic *ab initio* computations.

The tests have shown that the weighting scheme works quite well when it is used in combination with theoretical X-ray diffraction data corresponding to electron densities of single atoms/molecules in large unit cells, while it is not effective when applied to experimental structure-factor amplitudes. The reason is that, for experimental data, the high-angle reflections are not as numerically dominant as in the single-atom/molecule cases and, moreover, the starting discrepancies between calculated and reference structure-factor amplitudes are more uniform across the different resolution ranges. Concerning the tests with X-ray diffraction data resulting from periodic *ab initio* calculations, we have seen that the weighting scheme gives similar results to those obtained with experimental data when we exploit the same number of structure-factor amplitudes, while it performs better when the number of reflections used as restraints increases. This can be seen as a consequence of the fact that, as the number of structure-factor amplitudes becomes larger, the situation is more similar to the cases of single-atom/molecule electron densities in large unit cells, both in terms of reflection distribution and in terms of starting discrepancies between calculated and reference X-ray diffraction data.

Therefore, based on the obtained results, we believe that the proposed weighting scheme could be profitably exploited in XRW calculations with structure-factor amplitudes resulting from gas-phase *ab initio* computations. This could be particularly useful if the Jayatilaka approach is exploited to extract exchange-correlation potentials from highly correlated *ab initio* electron densities (Genoni & Macetti, 2022). Furthermore, considering that the performance of the weighting scheme improves when the number of restraints increases, we also envisage its application when a large number of X-ray diffraction data must be used in XRW calculations. For instance, this would be the case if we imagine a future coupling of the Jayatilaka approach with X-ray free-electron laser (XFEL) data, for which we do not have discrete Bragg peaks but a continuous pattern in momentum space. In contrast, at present, we do not recommend the use of the weighting scheme when usual experimental X-ray diffraction measurements are exploited in XRW computations, even when high-resolution data for charge-density studies are available. In fact, in those situations, convergence problems would be highly probable, and, above all, the use of the reflection weights would lead to worse fittings of the experimental data compared with a traditional XRW calculation. In our opinion, similar problems might likewise be encountered if, by exploiting experimental reflections, we attempted to carry out XRW calculations with a specific external $\lambda_J$ parameter for each resolution region.

## Acknowledgements

The authors are grateful to Piero Macchi (Politecnico di Milano, Italy) for helpful discussions and suggestions, and Fabien Pascale for the set-up and maintenance of the LPCT cluster, which was used to perform most of the calculations reported in this paper.

## Funding information

The following funding is acknowledged: Agence Nationale de la Recherche (grant No. ANR-17-CE29-0005-01 to Alessandro Genoni).

## References

Bader, R. F. W. (1990). *Atoms in Molecules: a Quantum Theory*. Oxford: Clarendon Press.
Bader, R. F. W. & Gatti, C. (1998). *Chem. Phys. Lett.* **287**, 233–238.
Becke, A. D. & Edgecombe, K. E. (1990). *J. Chem. Phys.* **92**, 5397–5403.
Birkedal, H., Madsen, D., Mathiesen, R. H., Knudsen, K., Weber, H.-P., Pattison, P. & Schwarzenbach, D. (2004). *Acta Cryst.* A**60**, 371–381.
Blanco, M. A., Martín Pendás, A. & Francisco, E. (2005). *J. Chem. Theory Comput.* **1**, 1096–1109.
Bučinský, L., Jayatilaka, D. & Grabowsky, S. (2016). *J. Phys. Chem. A*, **120**, 6650–6669.
Bytheway, I., Grimwood, D. J., Figgis, B. N., Chandler, G. S. & Jayatilaka, D. (2002). *Acta Cryst.* A**58**, 244–251.
Bytheway, I., Grimwood, D. J. & Jayatilaka, D. (2002). *Acta Cryst.* A**58**, 232–243.
Capelli, S. C., Bürgi, H.-B., Dittrich, B., Grabowsky, S. & Jayatilaka, D. (2014). *IUCrJ*, **1**, 361–379.
Casati, N., Genoni, A., Meyer, B., Krawczuk, A. & Macchi, P. (2017). *Acta Cryst.* B**73**, 584–597.
Cole, J. M. & Hickstein, D. D. (2013). *Phys. Rev. B*, **88**, 184105.
Davidson, M. L., Grabowsky, S. & Jayatilaka, D. (2022*a*). *Acta Cryst.* B**78**, 312–332.
Davidson, M. L., Grabowsky, S. & Jayatilaka, D. (2022*b*). *Acta Cryst.* B**78**, 397–415.
Dos Santos, L. H. R., Genoni, A. & Macchi, P. (2014). *Acta Cryst.* A**70**, 532–551.
Dovesi, R., Erba, A., Orlando, R., Zicovich–Wilson, C. M., Civalleri, B., Maschio, L., Rérat, M., Casassa, S., Baima, J., Salustro, S. & Kirtman, B. (2018). *WIREs Comput. Mol. Sci.* **8**, e1360.
Dovesi, R., Orlando, R., Erba, A., Zicovich-Wilson, C. M., Civalleri, B., Casassa, S., Maschio, L., Ferrabone, M., De La Pierre, M., D'Arco, P., Noël, Y., Causà, M., Rérat, M. & Kirtman, B. (2014). *Int. J. Quantum Chem.* **114**, 1287–1317.
Dovesi, R., Saunders, V. R., Roetti, C., Orlando, R., Zicovich-Wilson, C. M., Pascale, F., Civalleri, B., Doll, K., Harrison, N. M., Bush, I. J., D'Arco, P., Llunell, M., Causà, M. & Noël, Y. (2014). *CRYSTAL14 User's Manual.* Torino, Italy: University of Torino.
Ernst, M., Genoni, A. & Macchi, P. (2020). *J. Mol. Struct.* **1209**, 127975.
Frisch, M. J., Trucks, G. W., Schlegel, H. B., Scuseria, G. E., Robb, M. A., Cheeseman, J. R., Scalmani, G., Barone, V., Mennucci, B., Petersson, G. A., Nakatsuji, H., Caricato, M., Li, X., Hratchian, H. P., Izmaylov, A. F., Bloino, J., Zheng, G., Sonnenberg, J. L., Hada, M., Ehara, M., Toyota, K., Fukuda, R., Hasegawa, J., Ishida, M.,

Nakajima, T., Honda, Y., Kitao, O., Nakai, H., Vreven, T., Montgomery, J. A. Jr, Peralta, J. E., Ogliaro, F., Bearpark, M., Heyd, J. J., Brothers, E., Kudin, K. N., Staroverov, V. N., Kobayashi, R., Normand, J., Raghavachari, K., Rendell, A., Burant, J. C., Iyengar, S. S., Tomasi, J., Cossi, M., Rega, N., Millam, J. M., Klene, M., Knox, J. E., Cross, J. B., Bakken, V., Adamo, C., Jaramillo, J., Gomperts, R., Stratmann, R. E., Yazyev, O., Austin, A. J., Cammi, R., Pomelli, C., Ochterski, J. W., Martin, R. L., Morokuma, K., Zakrzewski, V. G., Voth, G. A., Salvador, P., Dannenberg, J. J., Dapprich, S., Daniels, A. D., Farkas, Ö., Foresman, J. B., Ortiz, J. V., Cioslowski, J. & Fox, D. J. (2009). *Gaussian 09*, Revision D.01. Gaussian, Inc., Wallingford, Connecticut, USA.

Fugel, M., Malaspina, L. A., Pal, R., Thomas, S. P., Shi, M. W., Spackman, M. A., Sugimoto, K. & Grabowsky, S. (2019). *Chem. Eur. J.* **25**, 6523–6532.

Genoni, A. (2013*a*). *J. Phys. Chem. Lett.* **4**, 1093–1099.

Genoni, A. (2013*b*). *J. Chem. Theory Comput.* **9**, 3004–3019.

Genoni, A. (2017). *Acta Cryst.* A**73**, 312–316.

Genoni, A. (2020). *Acta Cryst.* A**76**, 172–179.

Genoni, A. (2022). *Acta Cryst.* A**78**, 302–308.

Genoni, A., Bučinský, L., Claiser, N., Contreras–García, J., Dittrich, B., Dominiak, P. M., Espinosa, E., Gatti, C., Giannozzi, P., Gillet, J.-M., Jayatilaka, D., Macchi, P., Madsen, A. Ø., Massa, L. J., Matta, C. F., Merz, K. M. Jr, Nakashima, P. N. H., Ott, H., Ryde, U., Schwarz, K., Sierka, M. & Grabowsky, S. (2018). *Chem. Eur. J.* **24**, 10881–10905.

Genoni, A., Dos Santos, L. H. R., Meyer, B. & Macchi, P. (2017). *IUCrJ*, **4**, 136–146.

Genoni, A., Franchini, D., Pieraccini, S. & Sironi, M. (2018). *Chem. Eur. J.* **24**, 15507–15511.

Genoni, A. & Macchi, P. (2020). *Crystals*, **10**, 473.

Genoni, A. & Macetti, G. (2022). In preparation.

Genoni, A., Macetti, G., Franchini, D., Pieraccini, S. & Sironi, M. (2019). *Acta Cryst.* A**75**, 778–797.

Genoni, A. & Meyer, B. (2016). *Adv. Quantum Chem.* **73**, 333–362.

Giannozzi, P., Andreussi, O., Brumme, Y., Bunau, O., Buongiorno Nardelli, M., Calandra, M., Car, R., Cavazzoni, C., Ceresoli, D., Cococcioni, M., Colonna, N., Carnimeo, I., Dal Corso, A., de Gironcoli, S., Delugas, P., DiStasio, R. A. Jr, Ferretti, A., Floris, A., Fratesi, G., Fugallo, G., Gebauer, R., Gerstmann, U., Giustino, F., Gorni, Y., Jia, J., Kawamura, M., Ko, H.-Y., Kokalj, A., Küçükbenli, E., Lazzeri, M., Marsili, M., Marzari, N., Mauri, F., Nguyen, N. L., Nguyen, H.-V., Otero-de-la-Roza, A., Paulatto, L., Poncé, S., Rocca, D., Sabatini, R., Santra, B., Schlipf, M., Seitsonen, A. P., Smogunov, A., Timrov, I., Thonhauser, T., Umari, P., Vast, N., Wu, X. & Baroni, S. (2017). *J. Phys. Condens. Matter*, **29**, 465901.

Grabowsky, S., Genoni, A. & Bürgi, H.-B. (2017). *Chem. Sci.* **8**, 4159–4176.

Grabowsky, S., Genoni, A., Thomas, S. P. & Jayatilaka, D. (2020). *21st Century Challenges in Chemical Crystallography II – Structural Correlations and Data Interpretation*, Structure and Bonding, Vol. 186, edited by D. M. P. Mingos & P. Rathby, pp. 65–144. Cham: Springer Nature.

Grabowsky, S., Jayatilaka, S., Mebs, S. & Luger, S. (2010). *Chem. Eur. J.* **16**, 12818–12821.

Grabowsky, S., Luger, P., Buschmann, J., Schneider, T., Schirmeister, T., Sobolev, A. N. & Jayatilaka, D. (2012). *Angew. Chem. Int. Ed.* **51**, 6776–6779.

Grabowsky, S., Weber, M., Jayatilaka, D., Chen, Y.-S., Grabowski, M. T., Brehme, R., Hesse, M., Schirmeister, T. & Luger, P. (2011). *J. Phys. Chem. A*, **115**, 12715–12732.

Grimwood, D. J., Bytheway, I. & Jayatilaka, D. (2003). *J. Comput. Chem.* **24**, 470–483.

Grimwood, D. J. & Jayatilaka, D. (2001). *Acta Cryst.* A**57**, 87–100.

Hansen, N. K. & Coppens, P. (1978). *Acta Cryst.* A**34**, 909–921.

Hickstein, D. D., Cole, J. M., Turner, M. J. & Jayatilaka, D. (2013). *J. Chem. Phys.* **139**, 064108.

Hudák, M., Jayatilaka, D., Perašínová, L., Biskupič, S., Kožíšek, J. & Bučinský, L. (2010). *Acta Cryst.* A**66**, 78–92.

Jayatilaka, D. (1998). *Phys. Rev. Lett.* **80**, 798–801.

Jayatilaka, D. (2012). *Modern Charge-Density Analysis*, edited by C. Gatti & P. Macchi, pp. 213–257. Dordrecht: Springer Netherlands.

Jayatilaka, D. & Dittrich, B. (2008). *Acta Cryst.* A**64**, 383–393.

Jayatilaka, D. & Grimwood, D. (2004). *Acta Cryst.* A**60**, 111–119.

Jayatilaka, D. & Grimwood, D. J. (2001). *Acta Cryst.* A**57**, 76–86.

Jayatilaka, D., Munshi, P., Turner, M. J., Howard, J. A. K. & Spackman, M. A. (2009). *Phys. Chem. Chem. Phys.* **11**, 7209–7218.

Johnson, E. R., Keinan, S., Mori-Sánchez, P., Contreras-García, J., Cohen, A. J. & Yang, W. (2010). *J. Am. Chem. Soc.* **132**, 6498–6506.

Kleemiss, F., Dolomanov, O. V., Bodensteiner, M., Peyerimhoff, N., Midgley, L., Bourhis, L. J., Genoni, A., Malaspina, L. A., Jayatilaka, D., Spencer, J. L., White, F., Grundkötter-Stock, B., Steinhauer, S., Lentz, D., Puschmann, H. & Grabowsky, S. (2021). *Chem. Sci.* **12**, 1675–1692.

Kohout, M. (2004). *Int. J. Quantum Chem.* **97**, 651–658.

Landeros-Rivera, B., Contreras-García, J. & Dominiak, P. M. (2021). *Acta Cryst.* B**77**, 715–727.

Macchi, P. (2020). *Crystallogr. Rev.* **26**, 209–268.

Macchi, P. (2022). *Quantum Crystallography: Expectations versus Reality*. Cham: Springer.

Macetti, G. & Genoni, A. (2019). *J. Phys. Chem. A*, **123**, 9420–9428.

Macetti, G. & Genoni, A. (2020). *J. Chem. Theory Comput.* **16**, 7490–7506.

Macetti, G. & Genoni, A. (2021*a*). *Adv. Quantum Chem.* **83**, 269–285.

Macetti, G. & Genoni, A. (2021*b*). *J. Chem. Theory Comput.* **17**, 4169–4182.

Macetti, G. & Genoni, A. (2021*c*). *J. Phys. Chem. A*, **125**, 6013–6027.

Macetti, G., Macchi, P. & Genoni, A. (2021). *Acta Cryst.* B**77**, 695–705.

Macetti, G., Wieduwilt, E. K., Assfeld, X. & Genoni, A. (2020). *J. Chem. Theory Comput.* **16**, 3578–3596.

Macetti, G., Wieduwilt, E. K. & Genoni, A. (2021). *J. Phys. Chem. A*, **125**, 2709–2726.

Massa, L. & Matta, C. F. (2018). *J. Comput. Chem.* **39**, 1021–1028.

Pawlędzio, S., Malinska, M., Kleemiss, F., Grabowsky, S. & Woźniak, K. (2022*a*). *Inorg. Chem.* **61**, 4235–4239.

Pawlędzio, S., Malinska, M., Kleemiss, F., Grabowsky, S. & Woźniak, K. (2022*b*). *IUCrJ*, **9**, 497–507.

Ricardi, N., Ernst, M., Macchi, P. & Wesolowski, T. A. (2020). *Acta Cryst.* A**76**, 571–579.

Roversi, P., Irwin, J. J. & Bricogne, G. (1998). *Acta Cryst.* A**54**, 971–996.

Sakata, M. & Sato, M. (1990). *Acta Cryst.* A**46**, 263–270.

Silvi, B. & Savin, A. (1994). *Nature*, **371**, 683–686.

Smaalen, S. van & Netzel, J. (2009). *Phys. Scr.* **79**, 048304.

Stewart, R. F. (1976). *Acta Cryst.* A**32**, 565–574.

Stoll, H., Wagenblast, G. & Preuss, H. (1980). *Theor. Chim. Acta*, **57**, 169–178.

Thomas, S. P., Jayatilaka, D. & Guru Row, T. N. (2015). *Phys. Chem. Chem. Phys.* **17**, 25411–25420.

Wesołowski, T. A. (2008). *Phys. Rev. A*, **77**, 012504.

Wesolowski, T. A., Shedge, S. & Zhou, X. (2015). *Chem. Rev.* **115**, 5891–5928.

Wesolowski, T. A. & Warshel, A. (1993). *J. Phys. Chem.* **97**, 8050–8053.

Whitten, A. E., Jayatilaka, D. & Spackman, M. (2006). *J. Chem. Phys.* **125**, 174505.

Wieduwilt, E. K., Macetti, G. & Genoni, A. (2021). *J. Phys. Chem. Lett.* **12**, 463–471.

Woińska, M., Jayatilaka, D., Dittrich, B., Flaig, R., Luger, P., Woźniak, K., Dominiak, P. M. & Grabowsky, S. (2017). *ChemPhysChem*, **18**, 3334–3351.